Enhanced concrete crack closure with hybrid shape memory polymer tendons

Brunella Balzano [a,*], John Sweeney [b], Glen Thompson [b], Cristina-Luminita Tuinea-Bobe [b], Anthony Jefferson [a]

[a] Cardiff University, School of Engineering, Queen's Building, The Parade CF23AA, United Kingdom
[b] University of Bradford, Bradford BD7 1DP, United Kingdom

ABSTRACT

The paper presents a new healing system that uses pre-tensioned hybrid tendons to close cracks in cementitious structural elements. The tendons comprise an inner core, formed from aramid fibre ropes, and an outer sleeve made from a shape memory PET. During the manufacturing process, the inner core of a tendon is put into tension and the outer sleeve into compression, such that the tendon is in equilibrium. A set of tendons are then cast in a cementitious structural element and heat activated once cracking occurs. This triggers the shrinkage potential of the PET sleeve, which in turn releases the stored strain energy in the inner core. The tensile force thereby released applies a compressive force to the cementitious element, in which the tendons are embedded, that acts to close any cracks that have formed perpendicular to the axis of the tendons. Details of the component materials used to form the tendon are given along with the tendon manufacturing process. A set of experiments are then reported that explore the performance of three different tendon configurations in prismatic mortar beams. The results from these experiments show that the tendons can completely close 0.3 mm cracks in the mortar beams and act as effective reinforcement both before and after activation. A nonlinear hinge-based numerical model is also described, which is shown to be able to reproduce the experimental behaviour with reasonable accuracy. The model is used to help interpret the results of the experiments and, in particular, to explore the effects of slip at the tendon anchorages and the amount of prestress force that remains after activation. It is shown that, with two of the tendon configurations tested, over 75% of the prestress potential of the tendon remains after crack closure.

1. Introduction

It has long been known that cracking can reduce the service life of concrete structures and such cracking remains a problem, even in new structures [19]. A potential solution to this problem is to introduce engineered (autonomic) self-repair mechanisms into structural elements, which are able to heal cracks as they form [31]. Several approaches have been developed for endowing concrete with this self-repairing ability, including technologies that use embedded bacterial spores [12,27,61,38], micro- and macro- encapsulation of healing agents [42,20,62,52,2,55,59], and embedded vascular networks for supplying healing agents to damage zones [15,28]. A much fuller account of previous work on self-healing cementitious materials may be found in several literature review articles [60,11,18,51,65].

A very different approach to crack 'healing' is to embed shape memory bars or tendons into structural elements that, when activated, release a shrinkage potential that provides a crack-closure mechanism. Some investigators [48,30] have used shape memory alloy (SMA) bars for this purpose, sometimes in combination with fibre-reinforced polymers [3,33,64,66], whilst others have employed shape memory polymer (SMP) tendons [26,16,25,21,56,57].

SMA bars were shown to be highly effective as a combined crack-closure/post-tensioning system but these are generally more suited to specialist applications due to the relatively high cost of these bars. The latter (SMP), which used pre-oriented polyethylene terephthalate (PET), is more economic and was shown able to close cracks in plain concrete elements but the relatively small crack closure force proved inadequate to significantly reduce crack openings in reinforced concrete elements.

In addition, the shape memory polymer tendons used by Teall et al. [56–57] tend to reduce in strength and stiffness when activated, which makes them less effective as reinforcement after activation. In response to these deficiencies, a research programme has been undertaken aimed at developing a new type of hybrid SMP tendon. Specifically, the aim of the work was to develop tendons that generate larger crack closure forces than the SMP tendons of Teall et al. [56–57] and which provide a much higher level of post-activation reinforcement. An added benefit of this type of crack closure system is that it enhances autogenous healing. This is because when crack openings are 0.1 mm or less, the potential for autogenous healing increases greatly [47,25].

The new hybrid tendons comprise an inner core of aramid fibre (in this case Kevlar®) and an outer SMP sleeve formed from orientated PET. Aramid fibres are chemically stable and are characterised by their relatively high strength, light weight and thermal stability [45]. The use of aramid fibre tendons for prestressed concrete is well-established [8,9,10,5] and a number of structures have been built using this type of prestressing system [14]. Shape memory properties of orientated PET have been reviewed recently [6,22,23,53]. The particular case of PET has been studied by a number of investigators [24,39,41,44,50,63], who have shown that it is possible to create a variety of shapes of drawn PET with a shrinkage potential that can be activated by heating.

This paper gives details of research programme on the new hybrid tendons and also presents a numerical model that is used to help interpret the experimental results from tests on centrally-notched mortar beams. The model employs the concept of a nonlinear 'hinge', which represents the behaviour of the beam at the location of the notch [58,1]. In the present case, the hinge model was combined with layered beam theory [37].

The layout of the remainder of the paper is as follows. Section 2 presents the overall concept of the hybrid tendon and their action in a structural element, i.e. a beam. Section 3 gives details of the component materials of the tendon and the mortar mix and describes the tendon manufacturing process. Section 4 describes the test specimens and gives the experimental procedures. Section 5 presents the nonlinear hinge model. Section 6 gives the experimental results along with some discussion. Section 7 presents the main conclusions from the study.

2. General concept

The new hybrid tendon comprises two elements: the first is an outer cylinder (or sleeve) made of pre-drawn PET; the second consists of a prestressed core formed from Kevlar® rope. This pre-stressed core is restrained by the outer PET cylinder until the latter is activated, at which point the tensile pre-load in the core and the shrinkage potential of the cylinder are released. When the tendon is embedded and anchored in a concrete or mortar structural element, the release of this shrinkage potential results in a compressive force being applied to the structural element and this action tends to close any cracks that have formed perpendicular to the axis of the tendon. The concept underlying the tendon design is illustrated in Figs. 1 and 2.

Ideally, the tendon core should be a relatively high-strength low-modulus material. The high strength is required for prestressing and reinforcement and the low modulus minimises prestress losses due to creep and shrinkage in the mortar (or concrete). It is also important that the modulus is not so low as to compromise the post-activation reinforcement function of the tendons. The authors investigated various materials using mechanical beam idealisations and found that Kevlar® had the right combination of strength and stiffness.

The first manufacturing stage is the pre-tensioning of the inner cable, which is initially stressed elastically. Once the inner cable reaches the desired pre-stress, the whole system is locked using specific cable-grips tailored for the application (See Figs. 1 & 2).

At this point, the external force is released onto the inner core and the system is then in a self-equilibrated state, with the PET sleeve in compression and the core in tension, as previously illustrated in Fig. 1.
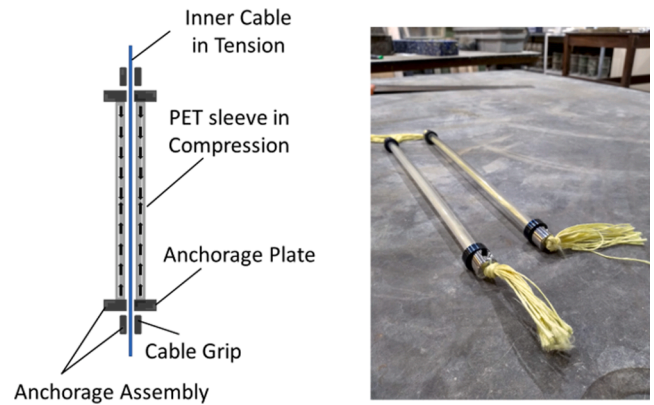

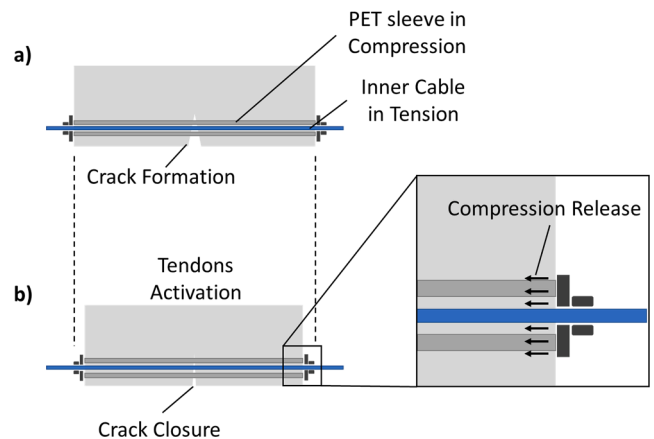**Fig. 1.** Hybrid tendon schematic and photograph.

Fig. 2. a) Hybrid tendons embedded in a structural element. b) Hybrid tendon activation and compression release.

The system is embedded in the cementitious structural element during casting, as explained in the next section. Once cracking has occurred, the hybrid tendon is activated via heating. This triggers the sleeve's shrinkage potential, thereby releasing the tensile force stored in the inner cable, which then applies a compressive force to the cementitious beam via the tendon's anchorages. In addition to post-tensioning the beam, the Kevlar® inner (core) cable also provides unbonded reinforcement both before and after activation. This gives the system the potential to entirely replace conventional reinforcement, which is contrast to a previous SMP-based system that did not provide reliable post-activation reinforcement [56].

It is emphasised that the tendons are designed to be unbonded between anchorages since this avoids high local tendon strains from developing in the vicinity of a crack [26], which could damage the tendon. Furthermore, this arrangement allows the full restrained shrinkage potential of the tendon to be available for closing cracks.

It is worth clarifying that the degree of autogenous healing effect was not explicitly measured in the experiments. Previous work has proven that this healing effect increases as crack widths decrease, with little healing occurring in cracks greater than 0.2 mm in width [47,25,17]. Since the present system closes serviceability-sized cracks, (e.g. from 0.2 mm to 0.01 mm), it may be stated with confidence that the system provides the crack opening conditions necessary for significant natural healing to take place.

3. Materials and tendon manufacture

3.1. Mortar mix

The cement mortar for the beam specimens was prepared using Portland cement CEM II A/L 32.5 R (CAS number 65997–15-1), standard quartz sand (CAS number 14808–100 60–7) as fine aggregate and tap water. Cement (c) and sand (s) were mixed in a c/s ratio of 1:3 by mass, and water (w) was added at a w/c ratio of 0.55 by mass. The mix proportions of cement, water and sand were 527.5 kg/m^3: 1582.4 kg/m^3: 290.1 kg/m^3 respectively. The sand was passed through a 2 mm sieve.

Three 100x100x100mm cubes and three 100x200mm cylinders were produced in order to perform compression and splitting tests in accordance with BS EN 12350–1:2000 and BS EN 12390–6:2009 respectively, with the aim of determining the compressive cube strength (f_{cu}) and tensile splitting strength (f_{cyl}) of the mortar paste. All the specimens were cured for 7 days prior to being tested. The compressive and splitting test results are given below in Table 1, noting that CV denotes the coefficient of variation.

It is noted that the true tensile strength (f_t) is approximately 0.85 f_{cyl}, (i.e. $f_t = 0.85 f_{cyl}$) and the true uniaxial strength (f_c) is approximately 0.8 f_{cu} (i.e. $f_c = 0.8 f_{cu}$) [34].

3.2. PET "sleeve"

The PET tubes were manufactured using a commercial grade of PET (Dow Lighter C93). This grade has been used to manufacture shape memory fibres [56] using a die-drawing process. This process has been adapted and developed for the production of tubes.

Firstly, tubes were extruded using the same Killion extruder as specified previously [56] in fibre manufacture. Operating conditions were set at a screw speed of 70 rpm, pressure of 200 bar, maximum extruder temperature 280 °C and die head temperature of 260 °C. Extrusion was through a circular section die of diameter 14 mm, with an internal pin of diameter 4 mm to create the central circular hole. The haul-off speed was 500 mm min^{-1} and final dimensions were outer diameter 13 mm and inner diameter 6 mm.

Then, the extruded tubes were die-drawn in 1 m lengths through a set of two dies: a converging die of 12 mm final diameter contacting the outside of the tube, inducing a small level of axial orientation; and a 30° conical diverging mandrel of final diameter 10 mm inside the tube. The purpose of the mandrel is to induce tangential or hoop orientation of the polymer. It was found that the balance between axial and hoop orientation produced by this process gave a higher compressive strength than that produced by axial orientation alone. Both the die and oven air temperatures were set at 90 °C. The initial haul-off speed was 40 mm min^{-1}, increasing during the die-drawing process to achieve steady conditions at 300 mm min^{-1}. The tube's final outer diameter was on average 8.7 mm, corresponding to a draw ratio of 4.0.

Adopting this manufacturing technique resulted in an improvement of the mechanical properties of the PET tubes. In particular, the compression strength, originally around 50 MPa, is now 90–100 MPa, which is enough to prevent the tube from crushing under the load of the inner cable. It should be noted that buckling is not an issue as a result of the design of the tendon, since the Kevlar® inner cable in tension prevents buckling of the outer cylinder.

The hybrid tendons used in this study had a length of 255 mm and the cross section shown in Fig. 3. The length was dictated by the size of
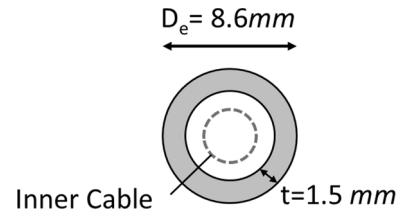
Table 1
Cube and cylinder strengths.

	f_{cu} (7 days) MPa	f_{cyl} (7 days) MPa
Mean	26.0	2.0
CV (%)	6.0	16.2

Fig. 3. Hybrid tendon cross section.

the mortar beams in which the tendons were embedded.

The shape memory response (or shrinkage potential) of PET sleeves is activated when they are exposed to a temperature of approximately 100 °C, and this shrinkage potential reaches a maximum at a temperature of between 120 and 130 °C. The free shrinkage response of six 50 mm long PET tubes are shown in Fig. 4. The tubes were activated by placing them in an oven at 130 °C for 30 min. As illustrated in the figure, the shrinkage strain varies between 8 and 15%.

The mechanical properties of the PET sleeve are reported in Table 2.

3.3. Kevlar® inner cable

Kevlar® is an organic fibre belonging to the family of the aramid fibres and is characterised by a relatively high tensile strength. The mechanical properties of the Kevlar material employed in this study are given in Table 3.

For this study, 4 mm and 2.3 mm diameter Parafil® Type F ropes made with DuPont™ Kevlar® brand fibre by the company Linear Composites were used.

4. Laboratory experiments

The performance of the hybrid tendons as a crack-closure system was tested by embedding them in 75x75x255mm mortar beams. The beams contained a central notch and were loaded in three-point bending, as shown in Fig. 5.

As a point of reference, the Eurocode 2 singly reinforced bending moment limit for a section of this size, with reinforcement placed at the average effective depth employed for this test, is 1.25kNm, which assumes that the mortar has the average strength given in Table 1 and that no partial factors are included. For the present beam configuration (Fig. 5), this equates to an applied load of 2.5kN, which is significantly higher than the load applied to any of the test specimens.

4.1. Tendon configurations

Three tendon configurations (series) were considered, as outlined below and illustrated in Fig. 6.

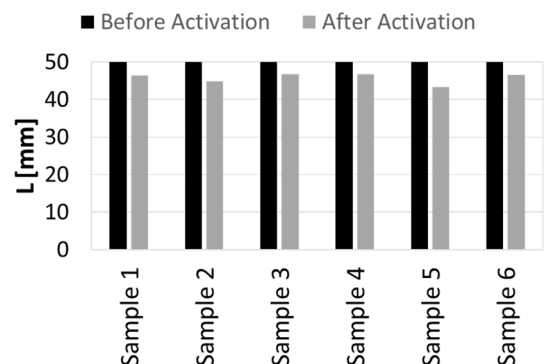Series 1: Two hybrid tendons were embedded in the mortar beams.

Fig. 4. Shrinkage potential of six 50 mm PET segments. The bar chart shows the lengths before and after the activation.

Table 2
PET mechanical properties.

		Average Value MPa	CV %
Tensile Strength	*MPa*	117.7	1.75
Compression Strength	*MPa*	84.07	9.78
Young Modulus	*MPa*	6472	1.45
Density	*kg/m³*	1380	1.52

Table 3
Kevlar® mechanical properties.

		Average Value MPa	CV %
Tensile Strength	*MPa*	740	11.4
Young Modulus	*MPa*	7023	0.96

The inner core of each tendon was made by combining 4 Parafil® ropes of 2.3 mm nominal diameter, which gives a relative core area ($A_{core}/(b \cdot h)$) of 0.15%. The tension force stored in each tendon after manufacture was approximately 600 N, giving a total initial pre-stressing force (P_{r0}) of 1200 N for the Series 1 configuration.

Series 2: Three hybrid tendons were embedded in the mortar beams. The inner core of each tendon was made by combining 2 Parafil® ropes of 4 mm nominal diameter, which gives a relative core area ($A_{core}/(b \cdot h)$)

of 0.45%. The tension force stored in each tendon after manufacture was approximately 750 N, giving a total initial pre-stressing force (P_{r0}) of 2250 N for the Series 2 configuration.

Series 3: Four hybrid tendons were embedded in the mortar beams. The inner core of each tendon was made by combining 2 Parafil® ropes of 2.3 mm nominal diameter and 2 ropes of 4 mm nominal diameter, which gives a relative core area ($A_{core}/(b \cdot h)$) of 0.6%. The tension force stored in each tendon after manufacture was approximately 900 N, giving a total initial pre-stressing force (P_{r0}) of 3600 N for the Series 2 configuration.

The initial configuration of the hybrid tendons (Series 1) was obtained using the classical flexural design approach for concrete beams. The required tendon area was calculated from the criterion that the activated tendons should induce an axial stress of approximately 0.5 MPa in the mortar at the lower surface level. This value was based on previous work [25,56] and was considered sufficient to achieve crack closure.

Once complete, the first test series was considered with the numerical model in a series of analyses. The results from these computations highlighted that tendon slippage was significant and detrimental to the performance of the system. A close inspection of the beams after the tests also confirmed that some slippage (~0.8 mm) had occurred at the anchorages. In addition, the results from the first series of tests suggested that a higher level of post-compression and a greater post-activation reinforcement (tendon) area would be beneficial. Hence, a series of simulations were undertaken to determine two further tendon
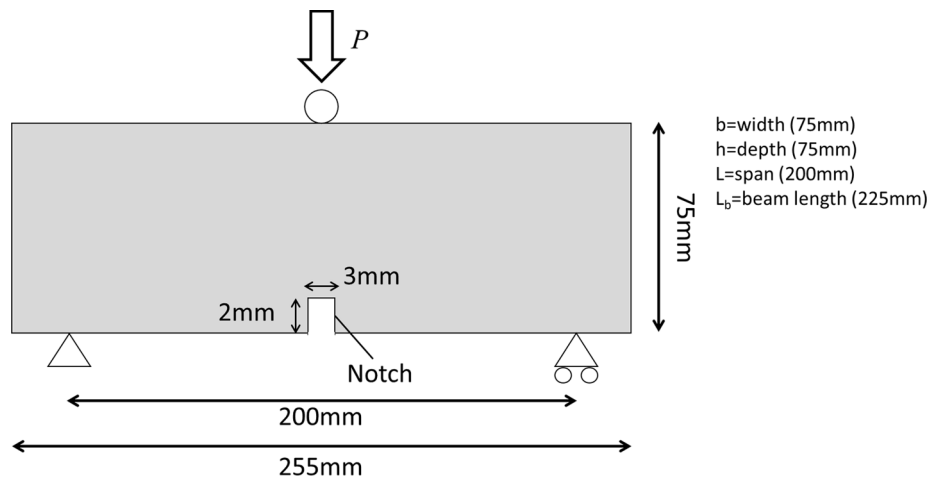

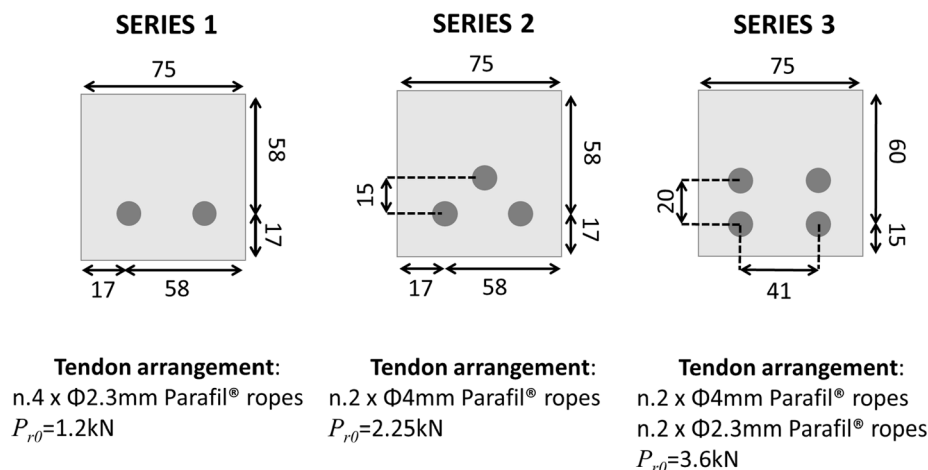**Fig. 5.** Mortar beam testing configuration.

Fig. 6. Tendon configurations.

configurations (See Fig. 6), which aimed to limit the amount of post-peak softening, increase the crack-closure and achieve a higher final load. The positions of the tendons in these configurations were based on the spacing requirements of the anchorages and mix compaction considerations. In addition, a minor -but effective- amendment was made to the anchorage fixing procedure, which involved additional anchorage clamps and ensuring that the clamping screw secured all of the strands adequately.

4.2. Common procedures

4.2.1. Specimen preparation

For each experiment, the hybrid tendons were positioned in wooden moulds designed specifically for this study (Fig. 7). A number of holes (2, 3 or 4) were drilled in the stop-ends in order to accommodate the tendons and anchorages, as illustrated in Fig. 7. The mortar paste was then poured into the mould in three layers, with each layer being compacted using a vibrating table.

Fig. 7 shows the preparation of the Series 1 to 3 specimens. For each case, one control beam was also prepared, which consisted of a plain mortar beam with no embedded elements. Beams with tendons are denoted SH beams (i.e. Self-Healing beams) in the remainder of this paper.
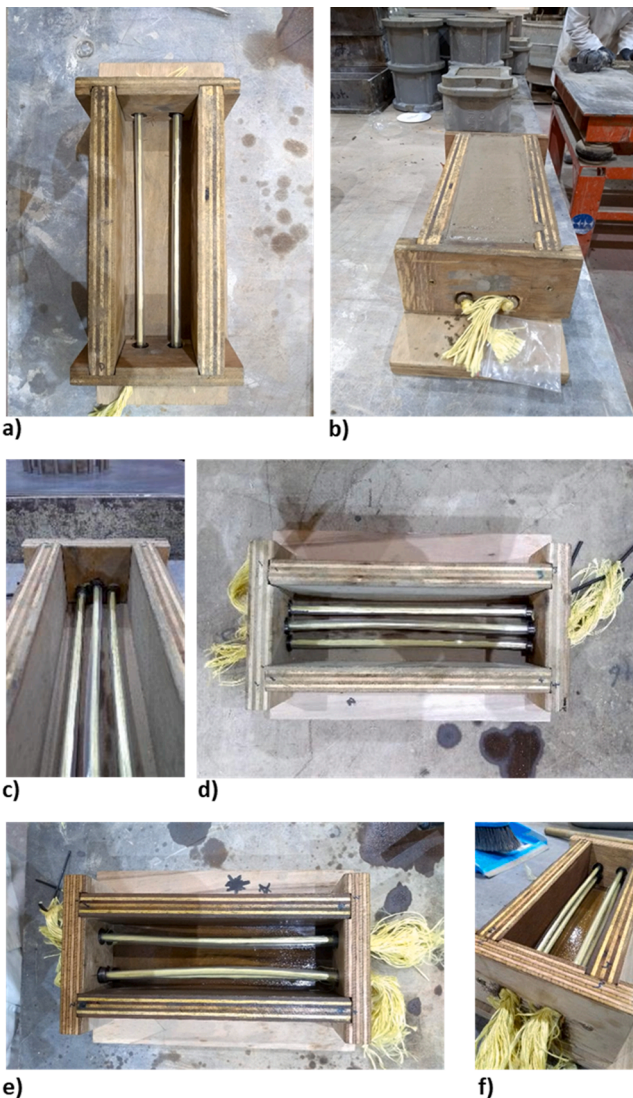

Fig. 7. Specimen preparation. a) Series 1; b) Series 2; c) Series 3.

After 24 h, the mortar beams were removed from the wooden moulds, covered in wet hessian and wrapped in cling film as shown in Fig. 8 a-b.

All the beam specimens were notched prior to testing, as illustrated in Figs. 5 and 9. Knife edge plates were then glued to the underside of the beam, as shown in Fig. 9a, to accommodate a lightweight clip gauge, which was used to measure the Crack Mouth Opening Displacement (CMOD) during the experiment (Fig. 9b).

4.2.2. Testing stages

The testing procedure comprised the following three stages, as illustrated in Fig. 10:

Stage 1. The specimen was subjected to three-point loading in order to induce a central crack. Once the crack opening reached the predetermined value, the specimen was then unloaded and removed from the loading machine. The aim of this initial stage was to induce a flexural crack in the mortar specimen.

Stage 2. The crack width was measured immediately after unloading and then the hybrid tendons were heat activated (See Section 4.2.4). The crack width was re-measured after activation, once the specimens had cooled to the ambient temperature. The crack width measurements are essential for proving the effective action of the hybrid tendons.

Stage 3. The mortar beam was then re-loaded in three-point bending to the maximum value the CMOD gauge could record prior failure. This stage aims to explore the post-compression effect on the crack-reopening behaviour.

4.2.3. Stage 1: Three - point bending Test.

The specimens were mounted in a Servicon Systems testing machine with a 100kN load cell and loaded in three-point bending, as illustrated in Fig. 11c. During the first stage of the test, the load was controlled via feedback from the CMOD clip gauge transducer, which allowed any softening behaviour to be captured. The initial CMOD rate was 0.0001 mm/s up to the first peak and then the rate was increased to 0.0003 mm/s until the end of the softening phase, at which point the rate was increased again to 0.0005 mm/s. The specimens were unloaded once the CMOD reached the designated value (i.e. 0.30, 0.35 and 0.40 mm for Series 1 specimens 1 to 3 respectively; and 0.3 mm for all Series 2 and 3 specimens) and then removed from the loading rig. The unloading rate was 0.0002 mm/s.

4.2.4. Stage 2: Crack aperture measurement and tendon's activation

Once a specimen had been removed from the loading rig, the crack width was measured in multiple locations using a magnifying camera, which was linked to an imaging software package. The beams were then placed in the oven at a temperature of 130° C for 45 mins in order to activate the tendons. Following activation, the crack width was remeasured in a number of locations.

4.2.5. Stage 3: Specimen reloading to failure and Kevlar® reinforcement

The specimens were then remounted in the same loading rig and retested in three-point bending until the CMOD reading reached the maximum value the sensor could record prior the failure of the mortar beam. This time, the initial CMOD rate was set to 0.0003 mm/s, which was increased to 0.0005 mm/s once the crack had visibly reopened.

5. Numerical model

A nonlinear beam-hinge model [58,1] was used to simulate the mechanical behaviour of the singly notched beams. The theory for the model is based on the assumption that inelastic deformations are confined to a narrow central zone of the beam, as illustrated in Fig. 11. The assumption is justified because cracking is generally confined to a narrow band of material above the notch and the stiffness of the cracking zone rapidly becomes significantly less than that of the surrounding material. This zone is termed a 'hinge' and may be associated with the
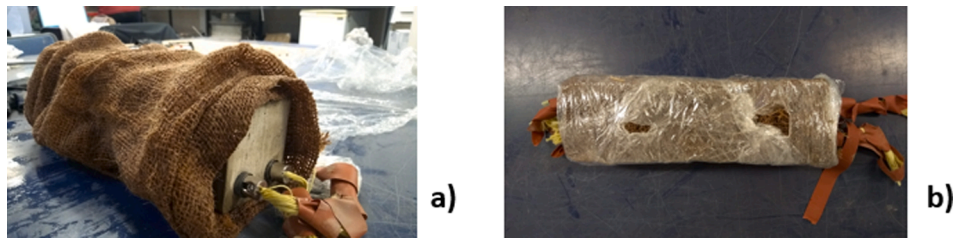
Fig. 8. Specimens during curing: a) specimen covered in wet hessian and b) wrapped in cling film.
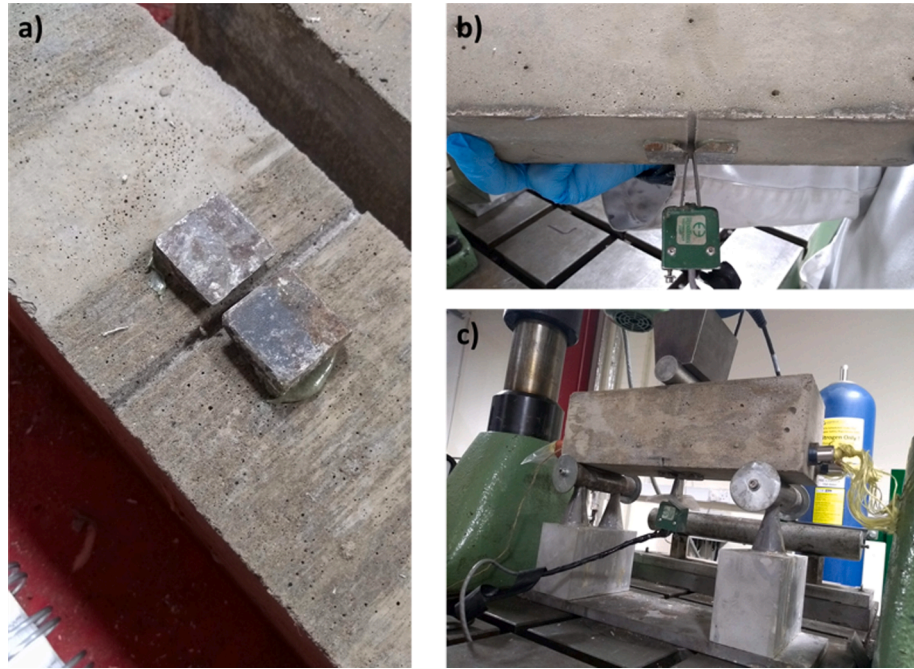

Fig. 9. Three-point bending testing arrangement. a) notch and knife edges b) clip gauge attached to the knife edges. c) beam mounted in the testing rig.
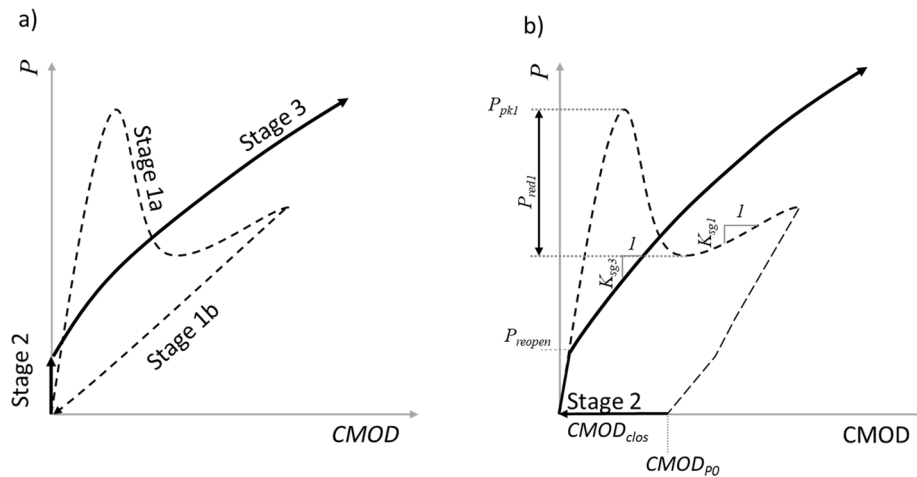

Fig. 10. a) Idealised load stages considered in the simulations: b) characteristic experimental response showing key experimental parameters.

fracture process zone [29] of the central crack. In this model, linear behaviour is assumed prior cracking and then, when the tensile stress in any layer within the hinge reaches the tensile strength of the material, cracking is initiated. The stress–strain response of each layer is then based on a damage model that simulates the characteristic strain softening behaviour of concrete, mortar and other quasi-brittle materials

[54,4]. This non-linear hinge theory has been used by a number of investigators to simulate the behaviour of beams formed of quasi-brittle materials [35,36,43].

Furthermore, it is assumed that the hinge zone may be simulated as a layered beam [37], which is under constant curvature and subjected to a uniform bending moment and normal force. The beam elements either
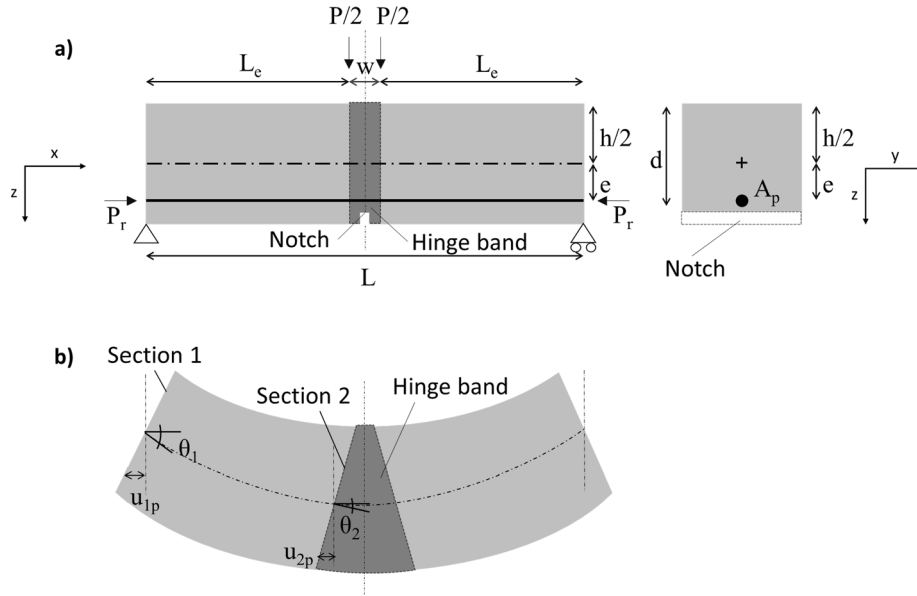
Fig. 11. Illustration of the non-linear hinge model.

side of the hinge zone are modelled using linear elastic beam elements. The layers within the hinge are assumed to be sufficiently narrow for the variation of axial strain within the depth of the layer (Δz) to be negligible, such that each beam layer can be represented with a uniaxial stress–strain constitutive relationship. The layered hinge zone is illustrated in Fig. 12.

The nonlinear stress–strain behaviour of each layer is represented using a one-dimensional version of the basic damage model presented by Alnaas and Jefferson [4], which may be expressed as equation (1).

$$\sigma = (1 - \omega(\zeta))E\varepsilon \tag{1}$$

in which σ and ε are the uniaxial stress and strain in a layer respectively, E is Young's modulus of the mortar, $\omega \in [0,1]$ is the scalar damage variable, which is a function of the effective strain (ζ), as follows;

$$\omega(\zeta) = \begin{cases} 0 & if \ \zeta < \varepsilon_t \\ 1 - \dfrac{\varepsilon_t}{\zeta}\left[e^{-c_1\left(\frac{\zeta-\varepsilon_t}{\varepsilon_0-\varepsilon_t}\right)}\right] & if \ \zeta \geq \varepsilon_t \end{cases} \tag{2}$$

where c_1 is a softening parameter (set to 5, as in Alnaas and Jefferson [4]); ε_0 is the strain at the end of the softening curve, may be expressed as $\varepsilon_0 = \frac{u_0}{w}$; u_0 is the displacement at the end of the softening curve (set to 0.3 mm in this work); and $\varepsilon_t = f_t/E$, where f_t is the tensile strength of the mortar.

The effective strain (ζ_i) for a layer i is defined as the maximum axial strain (ε_i) experienced in the layer up to the time being considered. ε_i is obtained using the following relationship:
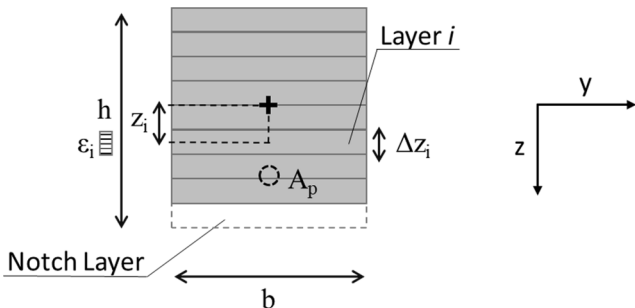

Fig. 12. Layered idealisation used for the hinge.

$$\varepsilon_i = \overline{\varepsilon} + \Psi_c z_i = \overline{\varepsilon} - \frac{2\theta_2}{w}z_i \tag{3}$$

where $\overline{\varepsilon}$ is the axial strain at $z = 0$ in the hinge; Ψ_c is the hinge curvature, θ_2 is the rotation at one edge of the hinge zone; w is the width of the hinge band and z_i is the vertical coordinate for layer i, as illustrated in Figs. 11 and 12.

The resultant axial force and moment associated with the hinge are obtained by integrating the stress, and the product of the stress and lever arm, respectively, over the hinge cross-section. In the present layered model, this is accomplished by summing the contributions from each layer, as follows;

$$N = \int_{-\frac{h}{2}}^{\frac{h}{2}} \sigma_c b dz = \left(\sum_i E_{ci} b_i \Delta z_i\right)\varepsilon_i = -P_r \tag{4a}$$

$$M = \int_{-\frac{h}{2}}^{\frac{h}{2}} \sigma_c b z dz = \frac{PL}{4} - P_r e \tag{4b}$$

where N and M are the axial force and moment resultants respectively; P is the applied load in three-point bending; P_r is the applied tendon force; b is the width of the mortar beam; L is the beam span; e is the eccentricity of the hybrid tendons system with respect to the centroid of the beam section.

The axial force and moment resultants are in equilibrium with the applied tendon force (P_r) and the applied external moment respectively, as shown in equations (4a) and (4b).

The tendon load is given by the following equation, which accounts for the pre-strain (ε_{p0}) and the horizontal displacement at the anchorage (u_{1p}), as illustrated in Fig. 13.

$$P_r = A_p E_p \left(\varepsilon_{p0} - \frac{2u_{1p}}{L}\right) \tag{5}$$

It is noted that ε_{p0} is zero prior to activation.

Introducing the elastic beam segments between the supports and the hinges, applying compatibility at the interface between these two components, employing equations (1) and (3), and applying symmetry leads to the following coupled nonlinear equations, in which the primary unknowns are $\overline{\varepsilon}$ and θ_2. The full derivation of the equations is presented in Appendix A.

$$\begin{bmatrix} N \\ M \end{bmatrix} = \begin{bmatrix} \sum_i E_{ci}b_i\Delta z_i + E_pA_p + \lambda_\varepsilon & \left(\sum_i E_{ci}b_iz_i\Delta z_i + z_iE_pA_p\right)\dfrac{2}{w} - \lambda_\theta \\ \sum_i E_{ci}b_iz_i\Delta z_i + E_pA_pz_p + \lambda_\varepsilon e & \dfrac{2}{w_c}\left(\sum_i E_{ci}b_iz_i{}^2\Delta z_i + E_pA_pz_p{}^2\right) - \lambda_\theta e \end{bmatrix} \cdot \begin{bmatrix} \overline{\varepsilon} \\ \theta_2 \end{bmatrix} \qquad (6)$$

with N and M being given by

$$\begin{bmatrix} N \\ M \end{bmatrix} = \begin{bmatrix} -(\lambda_{p0}\varepsilon_{p0} + \lambda_P P) \\ \dfrac{PL}{4} - (\lambda_{p0}\varepsilon_{p0} + \lambda_P P)e \end{bmatrix} \qquad (7)$$

where A_p is the area of the pre-stressed element, i.e. the cross section of the Kevlar® inner rope; E_p is Young modulus of the Kevlar® inner core; A_e is the area of the mortar beam outside the hinge band; E_e is Young modulus of the mortar outside the hinge band; $\lambda_{p0}, \lambda_\varepsilon, \lambda_\theta, \lambda_P, \kappa_1, \kappa_2, \kappa_3$ are variables given by the following expressions, as derived in Appendix A:

$$\lambda_{p0} = A_pE_p\left(1 - \frac{2}{L}\kappa_3\kappa_1\right) \qquad (8)$$

$$\lambda_\varepsilon = A_pE_p\frac{2}{L}\kappa_3\frac{w_c}{2} \qquad (9)$$

$$\lambda_\theta = -\left(A_pE_p\frac{2}{L}\kappa_3 e\right) \qquad (10)$$

$$\lambda_P = -\left(A_pE_p\frac{2}{L}\kappa_3\kappa_2\right) \qquad (11)$$

$$\kappa_1 = \frac{A_pE_pL_e}{E_e}\left(\frac{1}{A_e} + \frac{e^2}{I_e}\right) \qquad (12)$$

$$\kappa_2 = -\frac{e}{E_eI_e}\frac{L_e{}^2}{4} \qquad (13)$$

$$\kappa_3 = \frac{L}{L + 2\kappa_1} \qquad (14)$$

The model was coded in a Mathcad sheet (Mathcad 15.0 [32]), which was used for all of the numerical simulations reported in this paper. The associated algorithm follows the same three stages used in the testing procedure, as illustrated in Fig. 10. In terms of analysis stages, these are as follows;

Stage 1: Preloading to form a crack to a specified opening (1a) followed by unloading (1b);

Stage 2: Tendon activation and release of the post-tension force;

Stage 3: Reloading to the specified crack limit.

The nonlinear equations are solved using a standard Newton Raphson incremental iterative solution algorithm [13].

In Stage 1, the tendons are not yet activated, hence ε_{p0} is assumed to be zero; however, once the tendons are activated, ε_{p0} is released (hence $\varepsilon_{p0} \neq 0$) and there is a step increase in the force P_r (given by equation (5)).

The model was initially developed without allowing for any tendon slip at the anchorages, but it became apparent from the experimental responses and associated simulations that significant slip did occur. To allow this to be investigated, the model was modified by introducing a slip displacement. The path dependent total slip displacement at each anchorage (Δ_{slip}) was computed by summing the contributions from each stage up to -and including- the stage being considered;

$$\Delta_{slip} = \sum_{i=1}^{n_{stage}} \Delta_{slip,i} \qquad (15)$$

where n_{stage} is the number of the stage of the numerical modelling.

6. Results

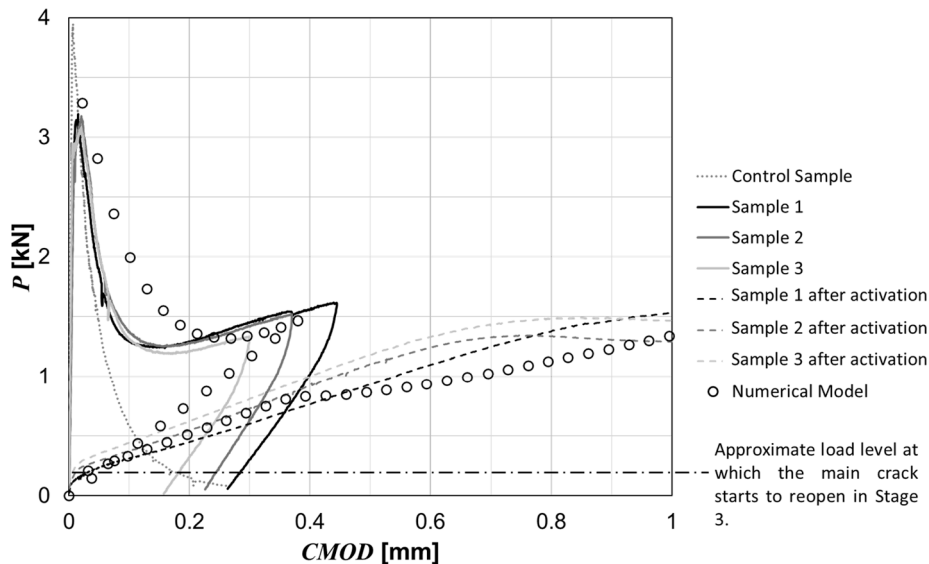The results from the three series of tests are now considered in detail.

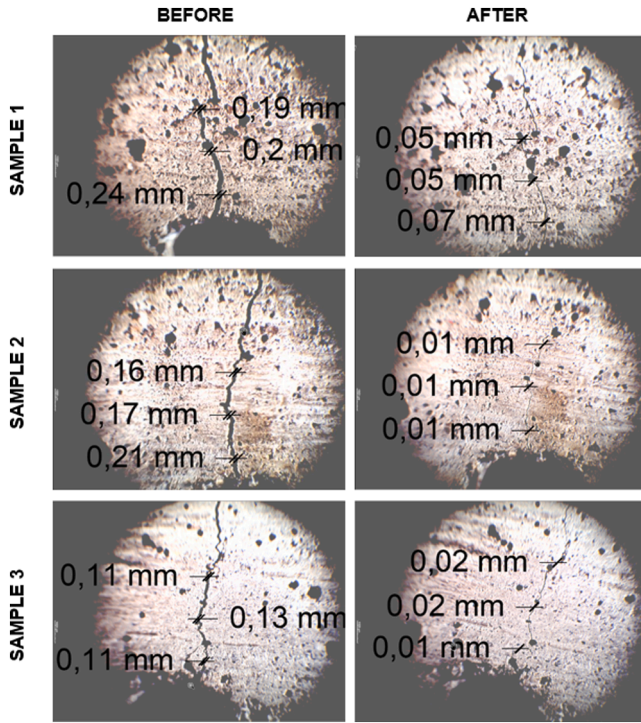Fig. 13. Load-CMOD responses of the Series 1 beams.

Fig. 14. Series 1. Crack wdth measurements before and after the hybrid tendons activation.

6.1. Series 1

The force-CMOD responses of the three Series 1 tests are given in Fig. 13. The response of all specimens exhibits quasi-linear behaviour until the peak load, after which the load reduces rapidly but then starts to rise again until the designated Stage 1 CMOD limit is reached. The first peak corresponds approximately to the point at which the first crack becomes visible and the post-peak softening behaviour is associated with the propagation of the primary crack. This softening response is initially consistent with that of a plain beam (i.e. a beam without tendons) but then the extension of the initially slack tendon reaches a level at which the tensile tendon force becomes significant. This tendon force

applies a hogging moment to the specimen at the anchorage positions, which counteracts the applied sagging moment and causes the applied load to rise.

As shown in Fig. 13, the specimens were loaded until the CMOD reached the designated value (denoted $CMOD_{stage1}$) before being unloaded. The $CMOD_{stage1}$ values used for samples 1, 2 and 3 were 0.3, 0.35 and 0.45 mm respectively. It is noted that different $CMOD_{stage1}$ values were chosen for each of the samples in Series 1 so that the effect of varying this parameter could be explored. In Series 2 and 3 the value of $CMOD_{stage1}$ was fixed at 0.3 mm, which is a typical serviceability crack opening limit.

When the selected CMOD value was reached, the specimens were unloaded. It is worth noting that for all of the samples the CMOD showed a non-zero value when the load was completely removed (denoted $CMOD_{P0}$, see Fig. 10) This permanent displacement is characteristic of concrete and mortar [46] and is attributed to the misalignment of, and friction between, opposing crack face asperities, as well as to particles that have broken off and fallen into the crack. It may be seen from Fig. 13 that $CMOD_{P0}$ increases with the value of $CMOD_{stage1}$, which implies that the wider the opening at unloading the more misalignment and debris there is in a crack. This trend would not be expected to continue beyond the point at which a crack is fully open.

Fig. 14 shows the crack width measured before and after tendon activation for the three samples. The crack width was measured at 1 mm, 3 mm and 5 mm from the notch on the front face of the mortar specimen. It is clear that the crack widths reduced substantially when the tendons were activated, with the final crack openings being well below the threshold value for significant autogenous healing [47,25].

The stage 3 responses of specimens 1 to 3 are shown on Fig. 13 with dotted lines. It may be seen that, in all cases, the initial reloading responses (up to 0.3 to 0.5kN) of the 3 specimens are relatively steep. The end of the initial reloading response coincides with when the primary crack starts to reopen, as annotated in Fig. 13. The reduced stiffness after the crack starts to reopen is nevertheless positive, which suggests that the tendon force increases as the beam deforms. The tangential stiffness (force-CMOD slope) remains positive because the combined stiffness of the anchored tendon and the uncracked mortar ligament always exceeded the reduction in stiffness caused by the reopening of the crack. However, the relatively low stiffness of the reloading response led the authors to suspect that there was slippage at the tendon anchorages.

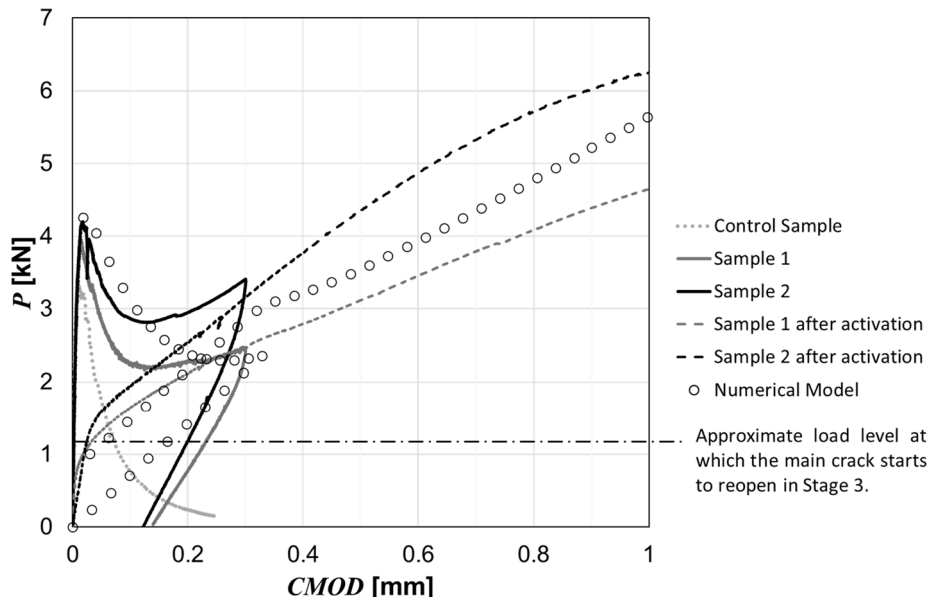In order to confirm this interpretation of the response, the numerical

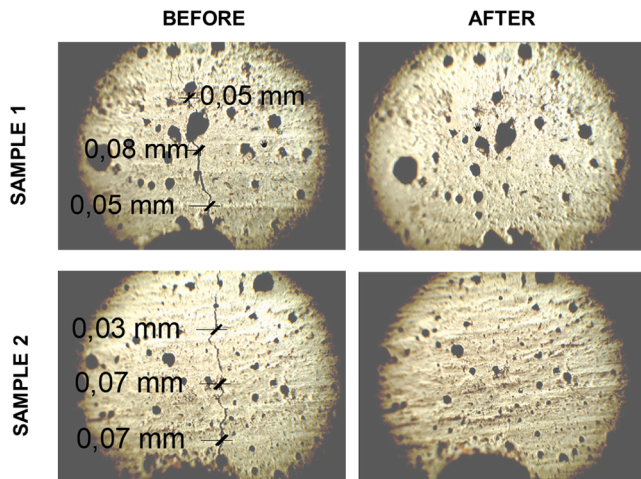**Fig. 15.** Load-CMOD graph for the Series 2 beams.

Fig. 16. Series 2. Crack wdth measurements before and after the hybrid tendons activation.

model was modified (see Section 5) and numerical simulations were undertaken of the specimens both with and without slip. This issue is discussed in more detail in Section 6.4.

6.2. Series 2

Three Series 2 mortar specimens were prepared together with a control beam but unfortunately one of the SH beams was damaged during manufacture and couldn't be tested any further. The force-CMOD responses of the SH and control specimens are given in Fig. 15.

The crack measurements before and after tendon activation are given in Fig. 16, which shows that the cracks were completely closed in both SH beams.

Comparing the crack openings after unloading (at the end of stage 1b) in Fig. 15 with the corresponding values before activation in Fig. 16 shows that the latter were all smaller than the former. This indicates that the cracks continued to close after the specimens had been demounted from the loading rig. This type of transient creep-like crack behaviour is known and results from residual stresses in the system, which comprise tensile stresses in the uncracked ligaments and balancing compressive

stresses across the crack face. This type of transient crack behaviour has been described using a visco-elastic rheological model by Santhikumar and Karihaloo [49].

Overall, the SH beams showed the same characteristic behaviour as those of the Series 1 beams except that the effects of the tendons were significantly greater in this case. This may be seen from the following observations, which are made relative to the response of the Series 1 beams;

   (i) less load reduction following the first peak (P_{red1});
  (ii) a higher stiffness in the post-softening section of stage 1, prior to unloading (K_{sg1});
 (iii) greater crack closure in stage 2 ($CMOD_{clos}$);
 (iv) higher crack reopening load in stage 3 (P_{reopen});
  (v) greater stiffness in the latter part of stage 3 (K_{sg3}).

Noting that the terms above in brackets are defined in Fig. 10 and quantified for all three series in Table 5 in Section 6.4. Section 6.4 also considers the effects of slip on this, and the other, test series.

6.3. Series 3

The Load CMOD responses and stage 3 crack closure measurements for the Series 3 tests are presented in Figs. 17 and 18 respectively. From Fig. 17, it is noticeable that very little softening occurs after the first peak in stage 1 of the tests and that the stage 1 post-softening (K_{stag1}) and stage 3 (K_{stag3}) stiffnesses are similar, which suggests that there was no significant initial slackness in the tendons in the case. Overall, the trends outlined in the five observations (i to v) made in Section 6.2, concerning the differences between the Series 1 and Series 2 beams, apply equally to the differences between the Series 2 and Series 3 beams. These trends are discussed further in the next section, which also considers the results of the numerical analyses.

6.4. Results from numerical analysis and discussion

The results from the numerical analyses for the three series of tests were presented along with experimental load-CMOD responses in Figs. 13, 15 and 17. The numerical responses are in generally good agreement with the experimental results and therefore are considered sufficiently reliable to help interpret the results.
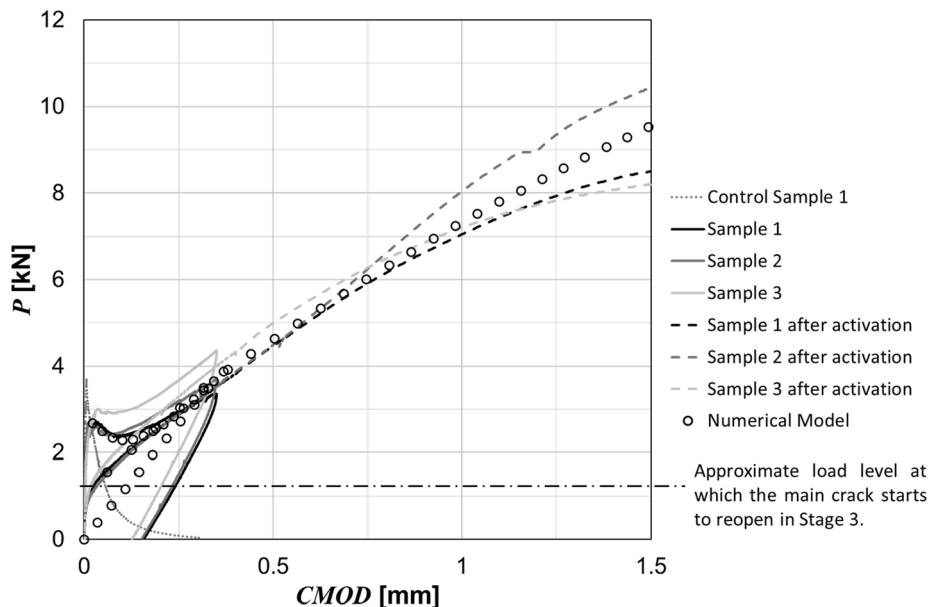

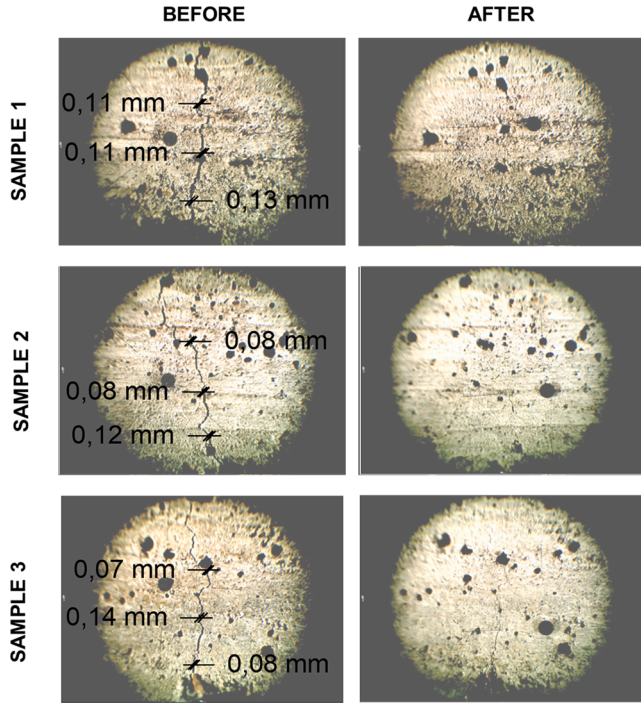**Fig. 17.** Load-CMOD graph for the Series 3 beams.

Fig. 18. Series 3. Crack wdth measurements before and after the hybrid tendons activation.

Fig. 19. Moment- Hinge Curvature diagrams for Series 1,2 and 3 which correspond to the sections in Fig. 6.

In Fig. 19 the Moment-Curvature diagrams of the hinge section ($2\,\theta_2/w_c$) for the three experimental series are shown, which reflect the load-CMOD responses seen in Fig. 13, 15 and 17.

Fig. 20 shows the distribution of the longitudinal component of stress in the mortar at the location of the hinge for the Series 3 beams, computed using the numerical model. Fig. 20a provides an overview of the stress distributions at different loading stages and Fig. 20b gives a series of expanded stress plots that highlight (i) the degree of damage (cracking) before activation, (ii) that the entire beam section is in compression immediately after tendon activation, (iii) that a crack has fully developed and that the compression zone is well into the plastic range by the time the peak load has been reached.

As mentioned in Section 6.1, the authors suspected that significant slippage was occurring at the anchorages, although the multi-strand nature of the tendon inner cores made it difficult to measure slip values accurately in the experiments. However, by calibrating the slip model described in Section 5 to the experimental data, it proved possible
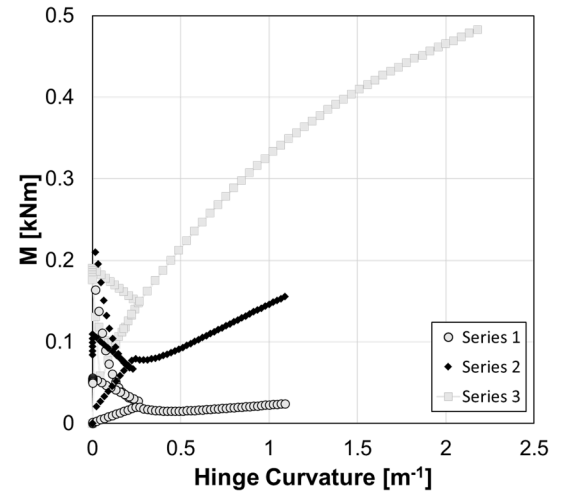
to compute the average tendon slip that occurred in each stage of each test series, as shown in Table 4. Table 4 also shows the calibrated effective pre-strain in each of the different tendons and the computed total tendon load at the end of each test (P_{r3}) and the associated stress in the tendon core (σ_{r3}). From the latter, it may be seen that the final stress in the Kevlar core was, in all cases, well below the strength of the material, i.e.740 MPa (See Table 3). This suggests that the Kevlar was not being used to its full potential at, or near, the ultimate limit state for this beam configuration.

The effect of slip is illustrated for the Series 3 beams in Fig. 21, which shows the results of an analyses with and without slip, in terms of applied load v CMOD response and the total tendon force v CMOD response. It is evident from these results that slip was a significant factor in governing the response of the beams.

Four parameters were identified in Section 6.2 that would be expected to vary with the size and number of the tendons, as well as with the amount of post-tensioning force; namely, P_{red1}, K_{sg1}, $CMOD_{clos}$, $P_{re-open}$, K_{sg3} (See Fig. 10). Another important factor, that gives a measure of the tendon efficiency, is the proportion of the original latent prestress force (P_{r0}) that remains after activation and crack closure. The tendon force after crack closure (P_{r-re}) may be determined in two ways; (i) by computing the total prestress force at the point at which the crack in stage 3 re-opens, (i.e. the value of P_r associated with P_{reopen} (P_{r-re})) assuming that the hinge behaves as an elastic section until the point of
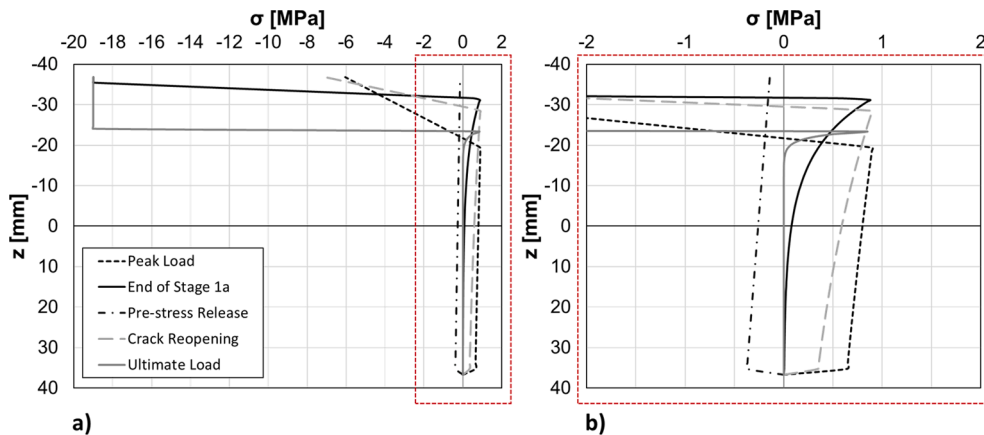

Fig. 20. Stress Distribution at the Hinge Section for Series 3. The stress graphs are reported at different stages of the three-point bending test. (Compression stresses are negative).

Table 4

Tendon slip, force and stress data.

	ε_{p0}	Δ_1	Δ_3	P_{r3}	σ_{r3}
	–	mm	mm	kN	MPa
SERIES 1	0.0009	0.09	0.77	1.32	79.5
SERIES 2	0.0013	0	0.17	6.16	81.7
SERIES 3	0.0007	0	0.38	12.90	96.4

Table 5

Experimental response parameters.

	P_{pk1}	P_{red1}	K_{sg1}	$CMOD_{clos}$	P_{reo}	K_{sg3}	P_{r-re}	P_{r0}	P_{r-re}/P_{r0}
	kN	kN	kN/mm	mm	kN	KN/mm	kN	kN	%
CONTROL	3.8[1]								
SERIES 1	3.2	1.8	1.3	0.21	0.15	1.5	0.3	1.2	25
SERIES 2	4.1	1.4	3.03	0.13[2]	1.2	4.0	2.0	2.25	89
SERIES 3	2.9	0.2	6.2	0.15[2]	1.4	6.2	2.8	3.6	78

Notes:

[1] average pf the peak value in the three control tests from the three tests series

[2] signifies100% crack closure in terms of measured CMOD
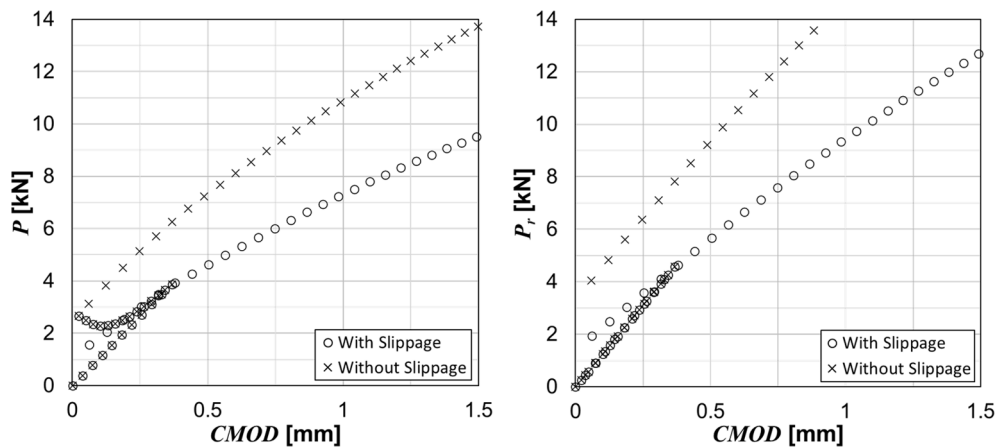
Fig. 21. Comparison between numerical simulations of the Series 3 beam with and without tendon slip.

incipient crack re-opening; (ii) directly from the numerical model. The tendon forces calculated by the two methods had similar answers (within 5%) and it is the values calculated using the numerical model that are given in Table 5. These values are those computed from the average of the tests in each series. For completeness, the average first peak load from each test set is also provided.

The first peak loads from the SH beams and control beams show a significant degree of variability (CV 6%) and the general trend is for P_{pk1} of the SH beams to be lower than the control, although the Series 2 results don't support this trend.

As may be expected, the stage 1 and 3 stiffnesses increase with the total tendon area and the amount of post-peak reduction (P_{red1}) decreases with increasing tendon area. The tendon configurations used in Series 2 and 3 resulted in the CMOD returning (effectively) to zero. It should be mentioned that the crack opening displacements measured by the CMOD clip gauge 3 mm below the bottom of the specimens are larger than the values measured on the surface of the specimens above the notch (i.e. the values shown in Figs. 14, 16 and 18).

It is very noticeable from the values given in the final column of Table 5, that a much greater proportion of the original prestress force is present after crack closure in the Series 2 and 3 SH beams that in the Series 1 beams. This is attributed to the greater degree of slip (See Table 4) that occurred in the first series of beam tests. It is believed that the reason for this is that the procedure used to secure the grips was refined and improved after the first series of tests.

The ability of the tendons (in the Series 2 and 3 configurations) to completely close cracks that had been opened to 0.3 mm, and to apply a significant compression force to the beam after activation suggests that the system would be able to close cracks from early age effects and construction loads. The strength and stiffness of the Kevlar core has also been shown able to provide reliable reinforcement.

Overall, it is concluded that the new tendons provide an effective combined crack closure reinforcement system for cementitious structural elements.

7. Conclusions and ongoing investigations

The principal conclusions from the work are as follows:

- The new hybrid tendon, which comprises and inner Kevlar rope and outer sleeve of drawn PET, has sufficient prestress potential to close serviceability level cracks in compact mortar beam specimens, when the inner core comprises 0.45% or more of the mortar beam cross-section.
- The tendons act as effective reinforcement both before and after activation and, when the relative core area is 0.6% or greater, all but eliminates post-crack softening behaviour even before the tendons are activated.
- Over 75% of the prestress potential of the tendon remains after the tendons are activated and the cracks are closed, for tendon configurations that have 0.45% and 0.65% relative core areas.

- Significant tendon slip occurred at the anchorages, which results in a loss of efficiency both at serviceability and ultimate load levels.

The issues being addressed in ongoing work include;

(i) the effective elimination of slip at the anchorages;
(ii) increasing the capacity of the PET sleeve and improving the manufacturing method for the tendons with the aim of increasing the prestress potential of the tendons;
(iii) seeking more cost-effective core materials, since it is acknowledged that Kevlar is relatively expensive;
(iv) redesigning the system such that a higher proportion of the core capacity is used at the ultimate limit state;
(v) allowing for permanent crack opening displacements in the model so that it better simulates the stage 2 crack closure response of the SH beams.
(vi) Adapting an existing activation system [57] for the hybrid tendons and testing the system in large-scale structural elements.

CRediT authorship contribution statement

Brunella Balzano: Conceptualization, Methodology, Software,

Investigation, Writing - original draft, Writing - review & editing, Visualization, Data curation. **John Sweeney:** Resources, Writing - review & editing. **Glen Thompson:** Resources, Investigation. **Anthony Jefferson:** Conceptualization, Methodology, Supervision, Software, Writing - review & editing, Project administration, Funding acquisition.

Declaration of Competing Interest

The authors declare that they have no known competing financial interests or personal relationships that could have appeared to influence the work reported in this paper.

Acknowledgement

Appendix

With reference to 13, when the structural element is loaded in three-point bending and the hybrid tendons are activated the equilibrium of the axial forces and momentum is expressed as follows;

$$N = \int_{-\frac{h}{2}}^{\frac{h}{2}} \sigma_c b dz = -P_r \tag{A1}$$

$$M = \int_{-\frac{h}{2}}^{\frac{h}{2}} \sigma_c b z dz = \frac{PL}{4} - P_r e \tag{A2}$$

The total tendon load (P_r) applied to the beam can be expressed as follows;

$$P_r = A_p E_p \left(\varepsilon_{p0} - \frac{2u_{1p}}{L} \right) \tag{A3}$$

The displacement u_{1p} at the beginning of the elastic section (x = 0) is given by;

$$u_{1p} = -\overline{\varepsilon_{3p}} \frac{w}{2} + \frac{P_r L_e}{A_e E_e} - \int_0^{L_e} \frac{M(x)e}{E_e I_e} dx \tag{A4}$$

where $\overline{\varepsilon_{3p}}$ is the strain mid-height strain in the hinge band and it can be expresses as follows;

$$\overline{\varepsilon_{3p}} = \overline{\varepsilon} - \frac{2\theta_2}{w} e \tag{A5}$$

By using A5 and A3 in A4,

$$u_{1p} = -\left(\overline{\varepsilon} - \frac{2\theta_2}{w_c} e \right) \frac{w}{2} - \frac{P_r L_e}{A_e E_e} + \int_0^{L_e} \frac{\left(\frac{P_x}{2} - P_r e \right) e}{E_e I_e} dx$$

$$u_{1p} = -\left(\overline{\varepsilon} - \frac{2\theta_2}{w_c} e \right) \frac{w}{2} - \frac{P_r L_e}{A_e E_e} + \frac{e}{E_e I_e} \left(\frac{PL_e^2}{4} - P_r e L_e \right)$$

$$u_{1p} = -\overline{\varepsilon} \frac{w_c}{2} + \theta_2 e - \frac{L_e}{A_e E_e} A_p E_p \left(\varepsilon_{p0} - \frac{2u_{1p}}{L} \right) + \frac{e}{E_e I_e} \frac{PL_e^2}{4} - \frac{e^2 L_e}{E_e I_e} A_p E_p \left(\varepsilon_{p0} - \frac{2u_{1p}}{L} \right)$$

$$u_{1p} = -\overline{\varepsilon} \frac{w_c}{2} + \theta_2 e - A_p E_p \left(\varepsilon_{p0} - \frac{2u_{1p}}{L} \right) \left(\frac{L_e}{A_e E_e} + \frac{L_e e^2}{E_e I_e} \right) + \frac{e}{E_e I_e} \frac{PL_e^2}{4} \tag{A6}$$

by introducing the following;

$$\kappa_1 = -\frac{A_p E_p L_e}{E_e} \left(\frac{1}{A_e} + \frac{e^2}{I_e} \right) \tag{A7}$$

$$\kappa_2 = +\frac{e}{E_e I_e}\frac{L_e^2}{4} \tag{A8}$$

$$\kappa_3 = \frac{L}{L + 2\kappa_1} \tag{A9}$$

and using A6, A7 and A8 in A5, the latter becomes;

$$u_{1p} = \kappa_3\left(-\frac{w_c}{\bar{\varepsilon}\,2} + \theta_2 e + \kappa_1\varepsilon_{p0} + \kappa_2 P\right) \tag{A10}$$

By using A10 in A3 the P_r expression becomes;

$$P_r = A_p E_p\left(\varepsilon_{p0} - \frac{2}{L}\kappa_3\left(-\frac{w_c}{\bar{\varepsilon}\,2} + \theta_2 e + \kappa_1\varepsilon_{p0} + \kappa_2 P\right)\right)$$

$$P_r = A_p E_p\varepsilon_{p0} - A_p E_p\frac{2}{L}\kappa_3\left(-\frac{w_c}{\bar{\varepsilon}\,2} + \theta_2 e + \kappa_1\varepsilon_{p0} + \kappa_2 P\right)$$

$$P_r = A_p E_p\varepsilon_{p0} + A_p E_p\frac{2}{L}\kappa_3\bar{\varepsilon}\frac{w_c}{2} - A_p E_p\frac{2}{L}\kappa_3\theta_2 e - A_p E_p\frac{2}{L}\kappa_3\kappa_1\varepsilon_{p0} - A_p E_p\frac{2}{L}\kappa_3\kappa_2 P$$

$$P_r = \varepsilon_{p0}\left(A_p E_p - A_p E_p\frac{2}{L}\kappa_3\kappa_1\right) - A_p E_p\frac{2}{L}\kappa_3\theta_2 e + A_p E_p\frac{2}{L}\kappa_3\bar{\varepsilon}\frac{w_c}{2} - A_p E_p\frac{2}{L}\kappa_3\kappa_2 P \tag{A11}$$

by introducing the following;

$$\lambda_{p0} = A_p E_p\left(1 - \frac{2}{L}\kappa_3\kappa_1\right) \tag{A12}$$

$$\lambda_\varepsilon = A_p E_p\frac{2}{L}\kappa_3\frac{w_c}{2} \tag{A13}$$

$$\lambda_\theta = -\left(A_p E_p\frac{2}{L}\kappa_3 e\right) \tag{A14}$$

$$\lambda_P = -\left(A_p E_p\frac{2}{L}\kappa_3\kappa_2\right) \tag{A15}$$

and therefore, the final expression of P_r is;

$$P_r = \lambda_{p0}\varepsilon_{p0} + \lambda_\varepsilon\bar{\varepsilon} + \lambda_\theta\theta_2 + \lambda_P P \tag{A16}$$

For the axial equilibrium

$$N = \int_{-\frac{h}{2}}^{\frac{h}{2}}\sigma_c b dz = -P_r \tag{A17}$$

By adopting the layered model, the cross section of the beam is divided in layers. Therefore, the integration can be approximated by the sum of the contribution of each layer in the beam section. Hence;

$$N = \int_{-\frac{h}{2}}^{\frac{h}{2}}\sigma_c b dz = \left(\sum_i E_{ci}b_i\Delta z_i + E_p A_p\right)\varepsilon_i \tag{A18}$$

For each layer the strain can be defined as follows

$$\varepsilon_i = \bar{\varepsilon} + \Psi_c z = \bar{\varepsilon} - \frac{2\theta_2}{w_c}z_i \tag{A19}$$

By combining A19 with A17 and A18, it results in the following

$$\left(\sum_i E_{ci}b_i\Delta z_i + E_p A_p\right)\left(\bar{\varepsilon} - \frac{2\theta_2}{w_c}z_i\right) = -\left(\lambda_{p0}\varepsilon_{p0} + \lambda_\varepsilon\bar{\varepsilon} + \lambda_\theta\theta_2 + \lambda_P P\right) \tag{A20}$$

And finally

$$\left(\sum_i E_{ci}b_i\Delta z_i + E_p A_p + \lambda_\varepsilon\right)\bar{\varepsilon} - \theta_2\left(\left(\sum_i E_{ci}b_i z_i\Delta z_i + z_i E_p A_p\right)\frac{2}{w_c} - \lambda_\theta\right) = -\left(\lambda_{p0}\varepsilon_{p0} + \lambda_P P\right) \tag{A21}$$

The same approximation applied in A18 is valid also for the Eq. A(2). Hence

$$M = \int_{-\frac{h}{2}}^{\frac{h}{2}}\sigma_c b z_i dz = \left(\sum_i E_{ci}b_i z_i\Delta z_i + E_p A_p z_p\right)\varepsilon_i = \frac{PL}{4} - P_r e \tag{A22}$$

By using A16 and A19 in A22

$$\left(\sum_i E_{ci}b_iz_i\Delta z_i + E_pA_pz_p\right)\left(\overline{\varepsilon} - \frac{2\theta_2}{w_c}z\right) = \frac{PL}{4} - (\lambda_{p0}\varepsilon_{p0} + \lambda_\varepsilon\overline{\varepsilon} + \lambda_\theta\theta_2 + \lambda_P P)e$$

$$\left(\sum_i E_{ci}b_iz_i\Delta z_i + E_sA_pz_p + \lambda_\varepsilon e\right)\overline{\varepsilon} - \left(\frac{2}{w_c}\left(\sum_i E_{ci}b_iz_i{}^2\Delta z_i + E_pA_pz_p{}^2\right) - \lambda_\theta e\right)\theta_2 = \frac{PL}{4} - (\lambda_{p0}\varepsilon_{p0} + \lambda_P P)e \tag{A23}$$

Finally, the coupled relationship between the generalised forces (axial load and moment) and deformations (mean strain and curvature) is given by]

$$\begin{bmatrix} N \\ M \end{bmatrix} = \begin{bmatrix} \sum_i E_{ci}b_i\Delta z_i + \lambda_\varepsilon & \left(\sum_i E_{ci}b_iz_i\Delta z_i + z_iE_pA_p\right)\frac{2}{w_c} - \lambda_\theta \\ \sum_i E_{ci}b_iz_i\Delta z_i + \lambda_\varepsilon e & \frac{2}{w_c}\left(\sum_i E_{ci}b_iz_i{}^2\Delta z_i + E_pA_pz_p{}^2\right) - \lambda_\theta e \end{bmatrix} \cdot \begin{bmatrix} \overline{\varepsilon} \\ \theta_2 \end{bmatrix} \tag{A24}$$

Appendix A. Supplementary data

Supplementary data to this article can be found online at https://doi.org/10.1016/j.engstruct.2020.111330.

References

[1] Abdalla HM, Karihaloo BL. A method for constructing the bilinear tension softening diagram of concrete corresponding to its true fracture energy 2004;10:597–604.

[2] Al-Tabbaa A, et al. First UK field application and performance of microcapsule-based self-healing concrete. Constr Build Mater. Elsevier Ltd 2019;208(2019):669–85. https://doi.org/10.1016/j.conbuildmat.2019.02.178.

[3] Alam MS, Youssef MA, Nehdi ML. Exploratory investigation on mechanical anchors for connecting SMA bars to steel or FRP bars. Materials and Structures/Materiaux et Constructions 2010;43(SUPPL. 1):91–107. https://doi.org/10.1617/s11527-010-9601-0.

[4] Alnaas WF, Jefferson AD. 'A smooth unloading-reloading approach for the nonlinear finite element analysis of quasi-brittle materials', Engineering Fracture Mechanics. Elsevier Ltd 2016;152:105–25. https://doi.org/10.1016/j.engfracmech.2015.04.018.

[5] Alwis KGNC, Burgoyne CJ. Statistical lifetime predictions for aramid fibers. J Compos Constr 2005;9(2):106–16. https://doi.org/10.1061/(ASCE)1090-0268(2005)9:2(106).

[6] Behl M, Lendlein A. Shape-memory polymers. Mater Today 2007;10(4):20–8.

[8] Burgoyne CJ. Properties of polyaramid ropes and implications for their use as external prestressing tendons. In: Naaman AE, Breen JE, editors. External prestressing in bridges. Detroit: American Concrete Institute; 1990. p. 107–24.

[9] Burgoyne CJ. Composites in civil engineering—state of the art in Europe. Struct. Eng. Int. (IABSE, Zurich Switzerland) 1999;99(4):267–73.

[10] Burgoyne CJ. Rational use of advanced composites in con- crete. Proc. Inst. Civ. Eng Struct. Build. 2001;146:253–62.

[11] De Belie N, Gruyaert E, Al-Tabbaa A, Antonaci P, Baera C, Bajare D, et al. Adv. Mater. Interfaces 2018;5:1800074. https://doi.org/10.1002/admi.201800074.

[12] De Muynck W, et al. Bacterial carbonate precipitation improves the durability of cementitious materials. Cem Concr Res 2008;38(7):1005–14. https://doi.org/10.1016/j.cemconres.2008.03.005.

[13] De Souza Neto EA, Peric D, Owen DRJ. Computational Methods for Plasticity: Theory and Applications. Print ISBN:9780470694527. John Wiley & Sons Ltd.; 2008.

[14] Dolan CW. Kevlar Reinforced Prestressing for Bridge Decks. Transp Res Rec 1994:1290.

[15] Dry C. Matrix cracking repair and filling using active and passive modes for smart timed release of chemicals from fibers into cement matrices. Smart Mater Struct 1994;3(2):118–23. https://doi.org/10.1088/0964-1726/3/2/006.

[16] Dunn SC, Jefferson AD, Lark RJ, Isaacs B. Shrinkage behavior of poly(ethylene terephthalate) for a new cementitious-shrinkable polymer material system. J Appl Polym Sci 2011;120(5):2516–26. https://doi.org/10.1002/app.33109.

[17] Edvardsen C. Water permeability and autogenous healing of cracks in concrete. ACI Mater. J. 1999;96:448–54.

[18] Ferrara L, et al. 'Experimental characterization of the self-healing capacity of cement based materials and its effects on the material performance: A state of the art report by COST Action SARCOS WG2', Construction and Building Materials. Elsevier Ltd 2018;167:115–42. https://doi.org/10.1016/j.conbuildmat.2018.01.143.

[19] Gardner D, et al. A survey on problems encountered in current concrete construction and the potential benefits of self-healing cementitious materials. Case Stud Constr Mater 2018;8:238–47. https://doi.org/10.1016/j.cscm.2018.02.002.

[20] Gilford J, et al. Dicyclopentadiene and sodium silicate microencapsulation for self-healing of concrete. J Mater Civ Eng 2014;26(5):886–96. https://doi.org/10.1061/(ASCE)MT.1943-5533.0000892.

[21] Hazelwood T, Jefferson AD, Lark RJ, Gardner DR. Eng. Struct. 2015;102:176.

[22] Hu J, et al. Recent advances in shape-memory polymers: Structure, mechanism, functionality, modeling and applications. Prog Polym Sci. Elsevier Ltd 2012;37(12):1720–63. https://doi.org/10.1016/j.progpolymsci.2012.06.001.

[23] Huang WM, Ding Z, Wang CC, Wei J, Zhao Y, Purnawali H. Mater. Today 2010;13:54.

[24] Iijima M, Kohda N, Kawaguchi K, Muguruma T, Ohta M, Naganishi A, et al. Effects of temperature changes and stress loading on the mechanical and shape memory properties of thermoplastic materials with different glass transition behaviours and crystal structures. Eur J Orthod 2015;37(6):665–70. https://doi.org/10.1093/ejo/cjv013.

[25] Isaacs B, et al. Crack healing of cementitious materials using shrinkable polymer tendons. Structural Concrete 2013;14(2):138–47. https://doi.org/10.1002/suco.201200013.

[26] Jefferson A, Joseph C, Lark R, Isaacs B, Dunn S, Weager B. A new system for crack closure of cementitious materials using shrinkable polymers. Cem Concr Res 2010;40(5):795–801. https://doi.org/10.1016/j.cemconres.2010.01.004.

[27] Jonkers HM, et al. Application of bacteria as self-healing agent for the development of sustainable concrete. Ecol Eng 2010;36(2):230–5. https://doi.org/10.1016/j.ecoleng.2008.12.036.

[28] Joseph C, et al. Experimental investigation of adhesive-based self-healing of cementitious materials. Mag Concr Res 2010;62(11):831–43. https://doi.org/10.1680/macr.2010.62.11.831.

[29] Karihaloo BL. Fracture Mechanics and Structural Concrete. UK: Addison Wesley Longman; 1995.

[30] Kuang Y, Ou J. Self-repairing performance of concrete beams strengthened using superelastic SMA wires in combination with adhesives released from hollow fibers. Smart Mater Struct 2008;17(2). https://doi.org/10.1088/0964-1726/17/2/025020.

[31] Li VC, Herbert E. Robust Self-Healing Concrete for Sustainable Infrastructure. J Adv Concr Technol 2012;10(6):207–18. https://doi.org/10.3151/jact.10.207.

[32] Mathcad 15.0. Copyright © 2011 Parametric Technology Corporation and/or Its Subsidiary Companies. All Rights Reserved.

[33] Nehdi M, Alam MS, Youssef MA. Development of corrosion-free concrete beam-column joint with adequate seismic energy dissipation. Eng Struct 2010;32(9):2518–28. https://doi.org/10.1016/j.engstruct.2010.04.020.

[34] Neville AM. Properties of Concrete. fifth ed. Pearson Education Limited, England: Trans-Atlantic Publications Inc.; 2012.

[35] Olesen JF. Fictitious crack propagation in fiber-reinforced concrete beams. J Eng mechanics 2001;127(3):272–80.

[36] Olesen JF, Østergaard L, Stang H. Nonlinear fracture mechanics and plasticity of the split cylinder test. Materials and Structures/Materiaux et Constructions 2006;39(4):421–32. https://doi.org/10.1617/s11527-005-9018-3.

[37] Owen DRJ, Hinton E. Finite elements in plasticity: theory and practice. Swansea: Pineridge Press Ltd; 1980.

[38] Paine K, Horne I, Tan L, Sharma T, Heath A, Cooper R, et al. Microencapsulated spores and growth media for self-healing mortars. In: Caspeele R, Taerwe L, Frangopol DM, editors. Life-Cycle Analysis and Assessment in Civil Engineering: Towards an Integrated Vision. London, U. K.: CRC Press; 2018. p. 2247–54.

[39] Park J, Yoo JW, Seo HW, Lee Y, Suhr J, Moon H, Koo JC, Choi HR, Hunt R, Kim KJ, Kim SH, Nam JD. Electrically controllable twisted-coiled artificial muscle actuators using surfacemodified polyester fibers. Smart Mater Struct 2017;26(3). https://doi.org/10.1088/1361-665X/aa5323.

[41] Park C, et al. Shape memory effect of poly(ethylene terephthalate) and poly(ethylene glycol) copolymer cross-linked with glycerol and sulfoisophthalate group and its application to impact-absorbing composite material. J Appl Polym Sci 2004;94(1):308–16. https://doi.org/10.1002/app.20903.

[42] Pelletier MM, et al. Self-healing concrete with a microencapsulated healing agent. Kingston, USA, (C): University of Rhode Island; 2010.

[43] Qing L, Shi X, Mu R, Lu Y. An analytical non-linear hinge model for predicting the fracture processes of cementitious composites. Theor Appl Fract Mech 2019;104 (May). https://doi.org/10.1016/j.tafmec.2019.102387.

[44] Raidt T, Schmidt M, Tiller JC, Katzenberg F. Crosslinking of Semiaromatic Polyesters toward High-Temperature Shape Memory Polymers with Full Recovery. Macromol Rapid Commun 2018;39(6):1700768. https://doi.org/10.1002/marc.201700768.

[45] Reashad Bin Kabir E, Nasrin Ferdous E. Kevlar-The Super Tough Fiber. International Journal of Textile Science 2013;1(6):78–83. https://doi.org/10.5923/j.textile.20120106.04.

[46] Reinhardt HW. Fracture Mechanics of an Elastic Softening Material Like Concrete. Heron 1984;29(2):1–42. https://doi.org/10.1023/A:1012235530463.

[47] Reinhardt HW, Jooss M. Permeability and self-healing of cracked concrete as a function of temperature and crack width. Cem Concr Res 2003;33(7):981–5. https://doi.org/10.1016/S0008-8846(02)01099-2.

[48] Sakai Y, Kitagawa Y, Fukuta T, Iiba M. Experimental study on enhancement of self-restoration of concrete beams using SMA wire. In: Proc SPIE 5057, Smart Structures and Materials 2003: Smart Systems and Nondestructive Evaluation for Civil Infrastructures; 2003. https://doi.org/10.1117/12.482680.

[49] Santhikumar S, Karihaloo BL. Time-dependent tension softening. Mech Cohesive-Frictional Mater 1996;1:295–304.

[50] Santo L, Bellisario D, Quadrini F. Shape Memory Behavior of PET Foams. Polymers 2018;10(2):115. https://doi.org/10.3390/polym10020115.

[51] Sidiq A, Gravina R, Giustozzi F. 'Is concrete healing really efficient? A review', Construction and Building Materials. Elsevier Ltd 2019;205:257–73. https://doi.org/10.1016/j.conbuildmat.2019.02.002.

[52] Souza L, Al-Tabbaa A. 'Microfluidic fabrication of microcapsules tailored for self-healing in cementitious materials', Construction and Building Materials. The Authors 2018;184:713–22. https://doi.org/10.1016/j.conbuildmat.2018.07.005.

[53] Sweeney J, et al. 'Modelling of loading, stress relaxation and stress recovery in a shape memory polymer', Journal of the Mechanical Behavior of Biomedical Materials. Elsevier 2014;37:12–23. https://doi.org/10.1016/j.jmbbm.2014.05.011.

[54] Su RKL, Chen HHN, Kwan AKH. Incremental displacement collocation method for the evaluation of tension softening curve of mortar. Eng Fract Mech 2012;88: 49–62. https://doi.org/10.1016/j.engfracmech.2012.04.005.

[55] Talaiekhozan A, et al. A Review of Self-healing Concrete Research Development. Journal of Environmental Treatment Techniques 2014;2(1):1–11.

[56] Teall O, et al. Development of high shrinkage polyethylene terephthalate (PET) shape memory polymer tendons for concrete crack closure. Smart Mater Struct. IOP Publishing 2017;26(4). https://doi.org/10.1088/1361-665X/aa5d66.

[57] Teall O, Pilegis M, Davies R, Sweeney J, Jefferson T, Lark R, et al. A shape memory polymer concrete crack closure system activated by electrical current. Smart Mater. Struct. 2018;27:075016. https://doi.org/10.1088/1361-665X/aac28a.

[58] Ulfkjær, J. P., Krenk, S. and Brincker, R. (2002) Analytical Model for Fictitious Crack Propagation in Concrete Beams, Journal of Engineering Mechanics. Aalborg: Dept. of Building Technology and Structural Engineering, Aalborg University. doi: 10.1061/(asce)0733-9399(1995)121:1(7).

[59] Van Belleghem B, et al. (2018) Chloride induced reinforcement corrosion behavior in self-healing concrete with encapsulated polyurethane. Cem Concr Res. Elsevier December 2017;113:130–9. https://doi.org/10.1016/j.cemconres.2018.07.009.#.

[60] Van Tittelboom K, De Belie N. Self-healing in cementitious materials-a review. Materials 2013;6. https://doi.org/10.3390/ma6062182.

[61] Vijay K, Murmu M, Deo SV. 'Bacteria based self healing concrete – A review', Construction and Building Materials. Elsevier Ltd 2017;152:1008–14. https://doi.org/10.1016/j.conbuildmat.2017.07.040.

[62] Wang JY, et al. 'Self-healing concrete by use of microencapsulated bacterial spores', Cement and Concrete Research. Elsevier Ltd 2014;56:139–52. https://doi.org/10.1016/j.cemconres.2013.11.009.

[63] Wang M, Zhang L. Recovery as a Measure of Oriented Crystalline Structure in Poly (ether ester)s Based on Poly(ethylene oxide) and Poly(ethylene terephthalate) Used as Shape Memory Polymers. J Polym Sci, Part B: Polym Phys 1999;37(2):101–12. https://doi.org/10.1002/(SICI)1099-0488(19990115)37:2<101::AID-POLB1>3.0. CO;2-X.

[64] Wierschem N, Andrawes B. Superelastic SMA-FRP composite reinforcement for concrete structures. Smart Mater Struct 2010;19(2). https://doi.org/10.1088/0964-1726/19/2/025011.

[65] Xue C, et al. A review study on encapsulation-based self-healing for cementitious materials. Structural Concrete 2019;20(1):198–212. https://doi.org/10.1002/suco.201800177.

[66] Zafar A, Andrawes B. Seismic behavior of SMA-FRP reinforced concrete frames under sequential seismic hazard. Eng Struct 2015;98:163–73. https://doi.org/10.1016/j.engstruct.2015.03.045.